

Near wall patch representation of wall bounded turbulence

Sean P. Carney¹, Björn Engquist^{1,2}, and Robert D. Moser^{2,3†}

¹Department of Mathematics, The University of Texas at Austin, TX 78712, USA

²Oden Institute for Computational Engineering and Sciences, The University of Texas at Austin, TX 78712, USA

³Department of Mechanical Engineering, The University of Texas at Austin, TX 78712, USA

(Received xx; revised xx; accepted xx)

Recent experimental and computational studies indicate that near wall turbulent flows can be characterized by universal small scale autonomous dynamics that are modulated by large scale structures. We formulate numerical simulations of near wall turbulence in a small domain localized to the boundary, whose size scales in viscous units. To mimic the environment in which the near wall turbulence evolves, the formulation accounts for the flux of mean momentum through the upper boundary of the domain. Comparisons of the model's two dimensional energy spectra and low order single-point statistics with the corresponding quantities computed from direct numerical simulations indicate that it successfully captures the dynamics of the small scale near wall turbulence.

Key words:

1. Introduction

Wall bounded turbulent flows are characterized by a separation of scales between the flow in the near wall region, in which mean viscous stresses play an important role, and the flow farther away from the wall, where mean viscous effects are largely negligible. This separation of scales is quantified by the friction Reynolds number $Re_\tau = \delta/\delta_\nu$, where δ is the characteristic length scale of the problem at hand, such as a channel half-width, a pipe radius, or a boundary layer thickness, and $\delta_\nu = \nu/u_\tau$ is the viscous length scale, where ν is the kinematic viscosity of the fluid, $u_\tau = \sqrt{\tau_w/\rho}$, τ_w is the mean wall shear stress, and ρ is the fluid density. Both the direct numerical simulation (DNS) and large eddy simulation (LES) of such wall bounded turbulent flows are expensive, as the spatial degrees of freedom required to resolve the near wall layer scale as $\mathcal{O}(Re_\tau^{2.5})$ and $\mathcal{O}(Re_\tau^2)$ for DNS and LES, respectively (Mizuno & Jiménez 2013). For a large class of flows of technological importance, this cost is prohibitive, even on modern high-performance computing systems.

Thanks to advances in experimental techniques and computational power, the understanding of the physics of wall bounded flows has increased greatly since the earliest investigations by Hagen (1839), Darcy (1854), and Reynolds (1895), and the later work by Millikan (1938). It is well known that there is an autonomous near wall cycle of self sustaining mechanisms (Jiménez & Moin 1991; Hamilton *et al.* 1995; Jeong *et al.* 1997), involving low and high speed streamwise velocity streaks and coherent structures

† Email address for correspondence: rmoser@oden.utexas.edu

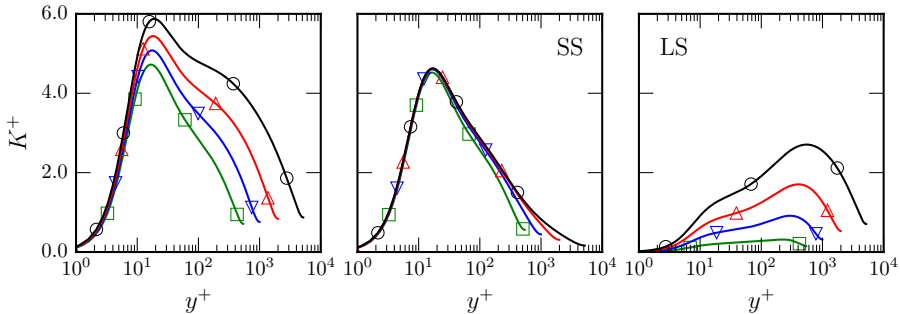


Figure 1: Unfiltered, high-pass (SS), and low pass (LS) portion of the turbulent kinetic energy scaled in viscous units with $k_{\text{cut}}\delta_\nu = 0.00628$ ($\lambda_{\text{cut}}/\delta_\nu = 1000$) for a channel flow at various Re_τ (green: $Re_\tau = 550$, blue: $Re_\tau = 1000$, red: $Re_\tau = 2000$, black: $Re_\tau = 5200$). The contributions from the large scales increases with Re_τ , but the contribution from the small scales is largely independent of Re_τ . Figure reproduced from Lee & Moser (2019) with permission.

of quasi-streamwise vorticity. Jiménez & Pinelli (1999) showed that this cycle of near wall dynamics persists without any input from the turbulence farther away from the wall. Moreover, if any element of the cycle is suppressed, the near wall turbulent kinetic energy (TKE) decays, and the flow becomes laminar. However, the large-scale structures in the outer layer do modulate the turbulent fluctuations in the near wall region (Hutchins & Marusic 2007; Marusic *et al.* 2010; Ganapathisubramani *et al.* 2012), leaving their “footprint” on the autonomous cycle. This results, for instance, in an Re_τ -dependent peak of the turbulent kinetic energy in the near wall region (see figure 1). Their influence increases with increasing Re_τ (DeGraaff & Eaton 2000).

Recently, Lee & Moser (2019) performed spectral analysis of channel flow DNS data for several different Re_τ (ranging from approximately 550 to 5200) to investigate the relative importance of different length scales to the production, transport, and dissipation of TKE. Their results suggest that the small scales in the near wall region behave universally. Indeed, when the spectrum of the TKE density is high-pass filtered to only include contributions from wavenumbers with magnitude larger than some $k_{\text{cut}}\delta_\nu = 0.00628$ (corresponding to a wavelength $\lambda_{\text{cut}}/\delta_\nu = 1000$), the resulting energy is found to be independent of Re_τ , as shown in figure 1. Similar results were also obtained in Samie *et al.* (2018) for experimental data ranging from $Re_\tau \approx 6000 - 20000$. These works, along with those mentioned above, indicate that the near wall region can be characterized by universal autonomous dynamics whose small scales are independent of Re_τ . The large scale portion of the near wall turbulence, however, is the result of eddies whose size and influence on the turbulent statistics depend on Re_τ .

With this understanding in mind, we endeavor to design a computational model of the universal small scales of turbulent, wall bounded flows in the case of a locally constant mean pressure gradient. The primary goal is to accurately represent the contribution of the small scales to the near wall turbulent statistics at a reduced cost relative to a DNS of the entire flow field. The model is formulated to simulate wall bounded turbulence only in a near wall, rectangular domain Ω localized to the boundary. The size of the domain scales in viscous units, so that as Re_τ increases, the domain shrinks in size relative to the size of the overall flow, but the number of computational degrees of freedom remains fixed. Assuming such a configuration can accurately model the dynamics of the near

wall, small scale features of the flow at a relatively low cost, it could be used to study the near wall statistics as a function of pressure gradient, covering, for instance, the cases of favorable, negligible and adverse pressure gradients.

This paper reports on the development and evaluation of just such a computational model of the near wall layer in turbulent shear flows. It originated as a design for the high-fidelity, “microscale” component of a multiscale computational approach for simulating wall bounded turbulence in the style of the heterogeneous multiscale method (Abdulle *et al.* 2012), as pursued by Sandham *et al.* (2017). Previous multiscale approaches of this type include Pascarelli *et al.* (2000) and Tang & Akhavan (2016), in which large eddy simulations are coupled to minimal flow unit simulations. The primary application target is to generate data to inform a pressure-gradient-dependent wall model for a large eddy simulation (Piomelli & Balaras 2002; Bose & Park 2018), as suggested by Coleman *et al.* (2015). A complementary approach using experimental data is the inner-outer predictive model developed by Mathis *et al.* (2011). Additionally, the model approach could potentially be used to study more complicated physics in the near wall region, such as heat transfer, chemical reactions, turbophoresis, or surface roughness.

The rest of the manuscript is organized as follows: section 2 contains a description of the computational model and the numerical method used to integrate the equations of motion. Section 3 provides a comparison between the statistics generated by the model and the corresponding quantities from DNS for the cases of both zero and mild favorable pressure gradients. In section 4 the results are summarized, and possible applications and extensions of the model are discussed.

2. Formulation

2.1. Notation

In the following discussion, the velocity components in the streamwise (x), wall-normal (y) and spanwise (z) directions are denoted as u , v , and w , respectively, and when using index notation, these directions are labeled 1, 2, and 3, respectively. The expected value is denoted with angle brackets (as in $\langle \cdot \rangle$), and upper case U and P indicate the mean velocity and pressure, so that $\langle u_i \rangle = U_i$. The velocity and pressure fluctuations are indicated with primes, e.g. $u_i = U_i + u'_i$. Partial derivatives shortened to ∂_i signify $\partial/\partial x_i$, differentiation in the direction x_i . The mean advective derivative is $D(\cdot)/Dt = \partial_t(\cdot) + U_j \partial_j(\cdot)$, where Einstein summation notation is implied. In general, repeated indices imply summation, with the exception of repeated Greek indices. Lastly, the superscript ‘+’ denotes non-dimensionalisation with the kinematic viscosity ν and the friction velocity u_τ .

2.2. Motivation: computational boundaries

The goal of the computational model is to simulate the turbulent small scales in the near wall region as a function of pressure gradient only in a small, rectangular domain localized to the boundary. This necessarily means placing nonphysical computational boundaries in a region of chaotic, highly nonlinear dynamics. In addition to the standard no-slip condition at the lower boundary $y = 0$, the use of periodic boundary conditions at the side-walls is well established, assuming the flow is statistically homogeneous in these directions. The problem of prescribing appropriate boundary conditions at the upper computational boundary, however, is nontrivial (Berselli *et al.* 2006; Sagaut *et al.* 2006). Once a mathematically well posed condition is prescribed, care must be taken to prevent the approximation inherent in the boundary condition from polluting the turbulent dynamics in the domain’s interior. To address this issue, the model augments

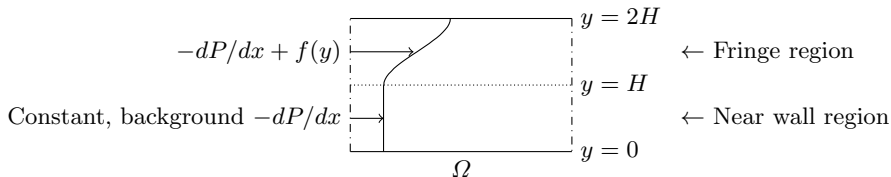


Figure 2: The fluid is subject to periodic boundary conditions at the (dash-dotted) side walls, constant Dirichlet/Neumann conditions at the upper boundary $y = 2H$, and the no-slip condition at the wall $y = 0$, as described in (2.1). In addition to the constant pressure gradient assumed to be present in the near wall layer, the model includes an auxiliary pressure gradient in a “fringe region” to account for momentum transport at the computational boundary $y = 2H$.

the near wall computational domain with a “fringe region.” In this fringe region, the flow is externally forced to account for the mean flux of momentum through the upper computational boundary that is precluded by the boundary conditions imposed there. The inclusion of such a region increases the computational cost of the model, but it provides the momentum transport needed to create the “correct environment” for the evolution of turbulence in the near wall region. In this way, the fringe region mollifies the effect of the nonphysical computational boundary. Similar techniques are used for designing inflow/outflow conditions in the DNS of turbulent boundary layers (Khujadze & Oberlack 2004; Colonius 2004; Wu & Moin 2009; Sillero *et al.* 2013), for example, as well as in molecular dynamics simulations, often referred to as a “heat-bath” or “thermostat” (Berendsen *et al.* 1984; Yong & Zhang 2013).

If one is interested in the turbulent statistics resulting from a constant pressure gradient near wall region out to a wall-normal height of $y \approx H$, the fringe region consists of a layer from $H \leq y \leq 2H$ in which a horizontally uniform streamwise forcing is applied, as illustrated in figure 2.

2.3. Mathematical formulation

The near wall patch (NWP) model is defined by the equations of motion and boundary conditions in the rectangular domain $\Omega = [0, L_x] \times [0, L_y] \times [0, L_z]$:

$$\left\{ \begin{array}{ll} \partial_t u_i + u_j \partial_j u_i + \partial_i p' - \nu \partial_j \partial_j u_i = f_i - \partial_i P & \text{in } \Omega \\ \partial_i u_i = 0 & \text{in } \Omega \\ \partial_i P = dP/dx \quad \delta_{i1} \text{ is constant} & \text{in } \Omega \\ u_i \text{ periodic in } x \text{ and } z \text{ directions} & \text{in } \Omega \\ u_i = 0 & y = 0 \\ v = \partial_y w = 0 & y = L_y \\ \partial_y u = \psi \in \mathbb{R} & y = L_y \\ f_i(x, y, z, t) = f(y) \delta_{i1} & \text{in } \Omega. \end{array} \right. \quad (2.1)$$

These are simply the forced incompressible Navier Stokes equations on a periodic domain in the wall-parallel directions, with the no-slip boundary condition at $y = 0$ (the wall), and no-flow through and constant viscous tangential traction $\nu \psi$ in the streamwise direction (x) specified at the top $y = L_y$. The term dP/dx models the mean pressure gradient in the real turbulent flow being modeled, while p' is the NWP model’s pressure field that evolves in time and space to maintain incompressibility. It only remains to

specify ψ and the forcing function $f(y)$. The former represents the viscous flux of mean momentum through the top, and the latter is a source of streamwise momentum that makes up for the missing turbulent flux of mean streamwise momentum through the upper computational boundary, owing to the boundary conditions that imply that the Reynolds stress vanishes there.

The forcing function $f(y)$ is non-zero only in the fringe region $y > L_y/2$, and is constructed such that

$$\int_0^{L_y} f(y) dy = -\tau_{\text{turb}}, \quad (2.2)$$

where τ_{turb} is the turbulent flux of mean momentum through $y = L_y$ in the turbulent flow being modeled.

In the real turbulent flow with a constant mean pressure gradient, the mean streamwise momentum equation integrated over $[0, L_y]$ yields:

$$-\frac{dP}{dx}L_y + \left(\nu \frac{\partial U}{\partial y} \Big|_{y=L_y} - \tau_{\text{turb}} \right) - \tau_w = 0 \quad (2.3)$$

$$\implies \tau_w = -\frac{dP}{dx}L_y + \tau_{\text{top}}, \quad (2.4)$$

where statistics are assumed to be homogeneous in both the stream and spanwise directions. The term in parentheses, τ_{top} , is the total momentum flux (viscous plus turbulent) through $y = L_y$, and it, along with dP/dx , determines the mean wall shear stress τ_w .

The mean streamwise stress balance for the NWP model system (2.1) is

$$\nu \frac{\partial U}{\partial y} - \langle u'v' \rangle + \int_0^y f(s)ds = y \frac{dP}{dx} + \tau_w. \quad (2.5)$$

The boundary conditions in (2.1) and the constraint (2.2) imply that at $y = L_y$, (2.5) becomes

$$\nu\psi + \int_0^{L_y} f(s)ds = L_y \frac{dP}{dx} + \tau_w \quad (2.6)$$

$$\implies \tau_w = -\frac{dP}{dx}L_y + \nu\psi - \tau_{\text{turb}}, \quad (2.7)$$

so that for fixed L_y , the parameters ν , τ_{turb} , ψ , and dP/dx determine τ_w . Dimensional analysis therefore implies that there is a two-parameter family of possible turbulent flows to model.

By specifying ψ and τ_{turb} so that $\nu\psi - \tau_{\text{turb}} = \tau_{\text{top}}$, the NWP model's mean stress balance augmented with the forcing function f (2.7) will be consistent with that of the real turbulent flow being modeled (2.4).

2.4. Physical parameters

The total mean stress at $y = L_y$ is given by

$$\tau_{\text{tot}} := \nu\psi - \tau_{\text{turb}}. \quad (2.8)$$

To scale the model in wall units, τ_{tot} is specified as a function of dP/dx to be

$$\tau_{\text{tot}} = 1 + L_y \frac{dP}{dx}, \quad (2.9)$$

Case name	NWP1000	NWP5200	NWPzpg
$-dP^+/dx^+$	$(1000.512)^{-1}$	$(5185.89)^{-1}$	0
τ_{tot}^+	0.4003	0.8843	1

Table 1: Prescribed mean pressure gradient and the resulting total momentum flux τ_{tot} at $y = L_y$ for the three model cases presented. The favorable pressure gradient parameters were selected to match the channel data posted at <https://turbulence.oden.utexas.edu/>.

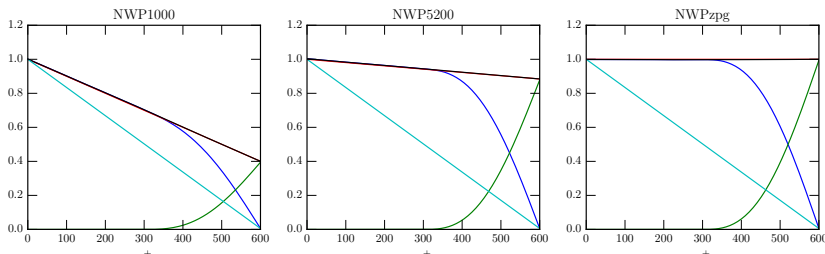


Figure 3: Blue: model total stress $\tau_{\text{model}}^+(y^+) = \partial U^+/\partial y^+ - \langle u'v' \rangle^+$; Red: target total stress $\tau_{\text{target}}^+ = 1 + y^+ dP^+/dx^+$; Green: Primitive $F^+(y^+)$ of forcing function f^+ ; Black: $\tau_{\text{model}}^+(y^+) + F^+(y^+)$; Cyan: total stress for a simulation *without* the forcing function f^+ ; for all the three model cases listed in table 1.

and the viscosity is set to $\nu = 1$. Note that (2.9) is simply the total mean stress for an equilibrium channel or boundary layer (Pope 2000).

The pressure gradient dP^+/dx^+ is thus one parameter defining a model case, and its values for the three cases presented—two favorable pressure gradient cases and one zero pressure gradient case—are shown in table 1. The values for τ_{tot}^+ are also shown for convenience, but of course they are simply determined via (2.9).

The second parameter to define a NWP model case is ψ^+ ; it determines the portion of τ_{tot}^+ that comes from mean viscous stress. For all of the statistics reported in section 3, however, the actual value of ψ^+ used was found to be insignificant. For each case listed in table 1, an initial ψ_{dns}^+ was determined from available DNS data. Results were then compared from runs with $\psi^+ = \psi_{\text{dns}}^+$, $\psi^+ = 2\psi_{\text{dns}}^+$, $\psi^+ = \psi_{\text{dns}}^+/2$, and $\psi^+ = 0$, and the differences were found to be negligible. Hence, there is really only a one-parameter family of possible turbulent flows to explore with the model, and for simplicity, ψ^+ is set to zero.

Figure 3 illustrates the statistically converged stress balances for these model cases. Included in the figure is a stress profile resulting from simulating the equations of motion (2.1) *without* the extra momentum flux provided by the auxiliary pressure gradient f (the cyan curve). In that case, a similar analysis to that shown in equations (2.5)–(2.7) above shows that the statistically converged stress profile is simply a linear function with values $\tau_w^+ = 1$ and ψ^+ at $y^+ = 0$ and $y^+ = L_y^+$, respectively. It is clear that this stress profile is in poor agreement with the target profiles (2.9), which is to be expected, since $\psi^+ = 1/(\kappa L_y^+)$ in the log-region. Moreover, this discrepancy increases with decreasing dP^+/dx^+ (corresponding to increasing Re_τ), illustrating the utility of including the extra momentum flux provided by the auxiliary forcing term f .

2.5. Computational parameters

The remaining model parameters, consistent for all three simulation cases, are summarized in table 2. The size of the rectangular domain Ω is taken to be $L_x^+ = L_z^+ = 1500$ and $L_y^+ = 600$; these values, while somewhat arbitrary, were determined through a combination of numerical experimentation and the results of Lee & Moser (2019). Their work suggests that the contributions to the turbulent kinetic energy from modes with wavelengths $\lambda^+ < 1000$ are universal and Re_τ -independent in a region below a wall-normal distance of approximately $y^+ = 300$. Accordingly, $L_y^+ = 2 \cdot 300 = 600$ is chosen to allow for a sufficiently large fringe-region to mollify the effect of the nonphysical computational boundary at $y = L_y$ (see figure 2), and both L_x^+ and L_z^+ are taken to be at least 1000.

For the domain size in the stream/spanwise directions, there generally is a balance between computational cost and the accuracy of the model, as defined by a comparison of the model's energy spectral density with that of large scale DNS. In particular, a variety of domain sizes were tested, ranging from $L_x^+ = L_z^+ = 1000$ to approximately 3500. Increasing L_x and L_z results in better agreement of the model's low-wavenumber, large-scale portion of the energy spectral density with the corresponding portion computed from DNS. The high-wavenumber, small-scale portion of the model's energy density, however, was insensitive to the domain size, so long as L_x and L_z were not taken to be too close to $L_x^+ = L_z^+ = 1000$. In particular, $L_x^+ = L_z^+ = 1500$ was found to be the smallest domain size capable of reproducing the universal small-scales discussed in section 3.3.

Given some target turbulent flux of mean momentum τ_{turb} , the auxiliary forcing f must satisfy (2.2), but it is otherwise unconstrained. For the simulations reported here, f is defined explicitly to be

$$f(y) = \begin{cases} 4\tau_{\text{turb}}/L_y^4 (L_y - 2y)^2 (5L_y - 4y), & y \in [L_y/2, L_y] \\ 0, & y \in [0, L_y/2], \end{cases} \quad (2.10)$$

which was chosen to satisfy $f(L_y/2) = f'(L_y/2) = f'(L_y) = 0$.

2.6. Numerical implementation and resolution

The model (2.1) is solved numerically using the velocity-vorticity formulation due to Kim *et al.* (1987). The equations of motion are discretized with a Fourier-Galerkin method in the stream/spanwise directions and a seventh order B-spline collocation method in the wall-normal direction (Kwok *et al.* 2001; Botella & Shariff 2003; Lee & Moser 2015). They are integrated in time with a low-storage, third order Runge-Kutta method that treats diffusive and convective terms implicitly and explicitly, respectively (Spalart *et al.* 1991). The numerical resolution in both space and time is consistent with that of DNS. The number of Fourier modes, and hence the numerical resolution, used in each simulation is listed in table 2, and can be compared with, for instance, table 1 in Lee & Moser (2015). In addition, the collocation point spacing in the wall-normal direction is similar to previous DNS studies; the total number of collocation points N_y is taken to be equal to the number of collocation points below $y^+ = 600$ in Lee & Moser (2015). They are then distributed in the near wall region according to the same (shifted and rescaled) stretching function.

The model is implemented with a modified version of the PoongBack DNS code (Lee *et al.* 2013, 2014), and the initial condition is taken from a restart file from a DNS run that is truncated to fit in Ω at the resolutions listed in table 2 and modified to satisfy the boundary conditions 2.1.

ψ^+	$L_x^+ = L_z^+$	L_y^+	N_x	N_z	N_y	Δx^+	Δz^+	Δy_w^+
0	1500	600	120	256	192	12.5	5.86	0.002817

Table 2: Summary of simulation parameters consistent for all simulation cases; ψ is the prescribed value for the Neumann boundary condition in (2.1). N_x and N_z refer to the number of Fourier modes, while N_y is the number of B-spline collocation points. $\Delta x = L_x/N_x$ and similarly for Δz . Δy_w is the collocation point spacing at the wall.

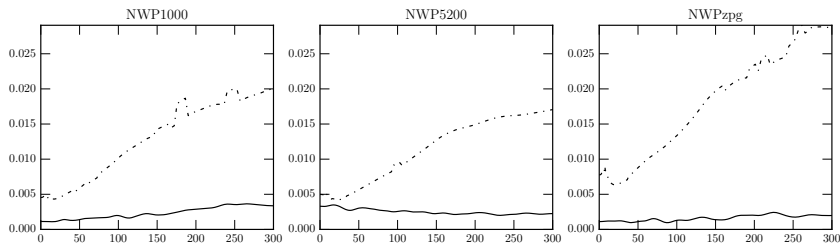


Figure 4: Statistical convergence for the model cases listed in table 2—solid lines: Absolute error $|\tau_{\text{model}}^+(y^+) - \tau_{\text{target}}^+(y^+)|$, where $\tau_{\text{model}}^+ = \partial U^+ / \partial y^+ - \langle u'v' \rangle^+$ and $\tau_{\text{target}}^+ = 1 + y^+ dP^+ / dx^+$; dashed lines: Standard deviation of the estimated statistical error for τ_{model}^+ in the region $y^+ \in [0, 300]$.

2.7. Statistical convergence

The method of Oliver *et al.* (2014) is used to assess the uncertainty in the statistics reported due to sampling noise. For each pressure gradient case, statistics are collected by averaging in time until the estimated statistical uncertainty in the mean stress profiles is less than a few percent. For the cases in table 2 reported here, the sampling error is less than three percent, as shown in figure 4.

3. Numerical results

The statistics reported here were computed from the three near wall patch model cases NWP1000, NWP5200, and NWPzpg and are compared to available DNS data. The favorable pressure gradient cases are compared to the corresponding channel flow DNS of Lee & Moser (2015, 2019) at $Re_\tau = 1000$ and $Re_\tau = 5200$ —referred to below as LM1000 and LM5200—whose statistics are available at <https://turbulence.ices.utexas.edu>. The zero pressure gradient case is compared to the turbulent boundary layer DNS of Sillero *et al.* (2013); Borrell *et al.* (2013); Simens *et al.* (2009); the data used for comparison corresponds to the streamwise location at which $Re_\tau = 2000$, and can be found at https://torroja.dmt.upm.es/turbdata/blayers/high_re/. It is referred to below as SJM2000.

3.1. Mean velocity and shear stresses

The most basic requirement of any model of near wall turbulence is to correctly capture the equilibrium velocity profile and the associated mean wall shear stress. Figure 5 demonstrates that the near wall patch (NWP) model’s mean velocity U^+ and log-law

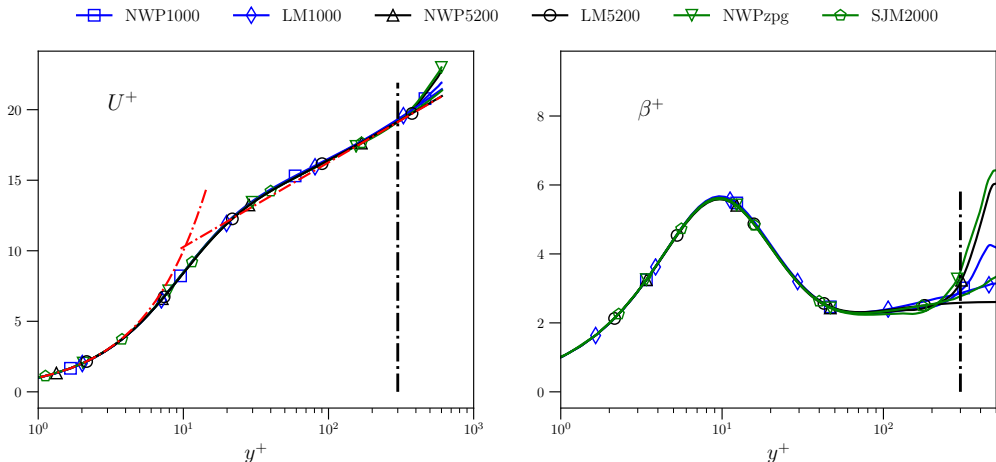


Figure 5: Mean velocity U^+ (left) and the indicator function $\beta^+ = y^+ \partial_{y^+} U^+$ (right) versus $\log(y^+)$. The black dashed-dotted vertical line marks $y^+ = 300$, and the red dashed-dotted lines plot the law-of-the-wall $U^+ = y^+$ and $U^+ = (1/\kappa) \log(y^+) + B$, where $\kappa = 0.384$ and $B = 4.27$ (Lee & Moser 2015).

indicator function

$$\beta^+(y^+) := y^+ \frac{\partial U^+}{\partial y^+} \quad (3.1)$$

agree with their DNS counterparts. The relative error in U^+ is less than 0.6% for $y^+ \in [0, 300]$, and the error is similarly small for β^+ in the range $y^+ \in [0, 100]$. However, there is mild disagreement of β in the range $y^+ \in [100, 300]$. As expected, the profiles diverge for $y^+ > 300$. The NWP model's Reynolds shear stress $\langle u'v' \rangle$ is in excellent agreement with that of the DNS in the region $y^+ \in [0, 300]$, as expected given the agreement of the mean velocity; see figure 6. For the channel cases, the error is less than 0.5%, and for the zero pressure gradient case the error is below 4%. In the former, the total stress at $y = L_y$ is known analytically as $\tau_{\text{tot}}^+ = 1 + L_y^+ dP^+/dx^+$ and is used to define $f(y)$ in (2.2), (2.8), and (2.9). In the latter, the same relations are used, though they are approximate due to the streamwise growth of the near wall layer in a boundary layer. This may explain the relatively larger discrepancy between the $\langle u'v' \rangle$ profiles for the boundary layer. In both instances, recall that $\langle u'v' \rangle$ necessarily vanishes at the upper computational boundary as a consequence of the boundary condition $v = 0$ in (2.1). The accuracy of the Reynolds shear stress profiles in spite of this condition demonstrates the utility of the forcing function f in enabling momentum transport to the near wall region $y^+ \in [0, 300]$.

3.2. Energy spectral density

For two points $(x, y, z), (x', y, z') \in \mathbb{R} \times [0, 2\delta] \times \mathbb{R}$ in an infinitely long channel, define the separation distances $r_x = x - x'$ and $r_z = z - z'$. For a turbulent flow that is statistically homogeneous in the stream and spanwise directions, the two point correlation tensor

$$R_{ij}(r_x, y, r_z) := \langle u'_i(x + r_x, y, z + r_z) u'_j(x, y, z) \rangle \quad (3.2)$$

is a function only of r_x, y , and r_z . Taking the Fourier transform of (3.2) in the variables r_x and r_z defines the spectral density $E_{ij}(k_x, y, k_z)$, which encodes the average contribution

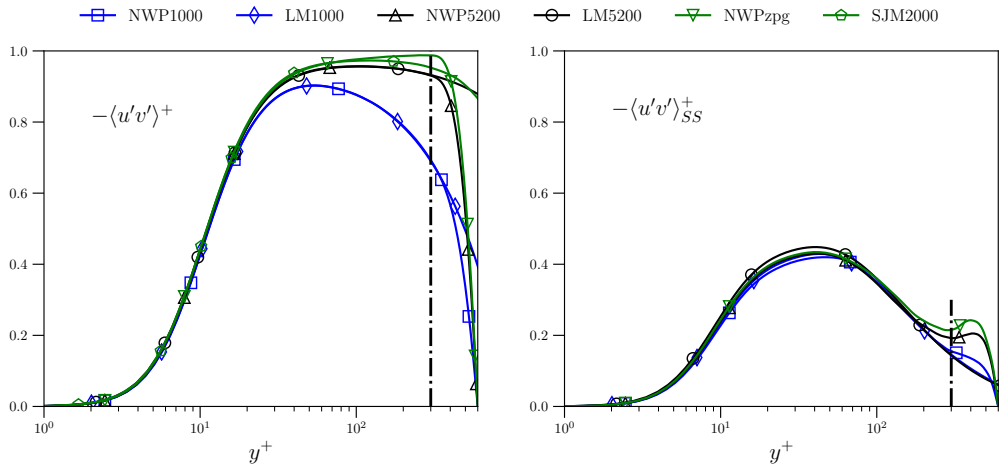


Figure 6: (a) Reynolds stress $-\langle u'v' \rangle^+$ and (b) the filtered Reynolds stress $-\langle u'v' \rangle_{SS}^+$ (defined by (3.8)) as a function of $\log(y^+)$, discussed in section 3.3. The black dashed-dotted vertical line marks $y^+ = 300$.

to the Reynolds stress tensor from different length scales as a function of the wall-normal variable y . The Reynolds stress tensor can be recovered by taking the limit $(r_x, r_z) \rightarrow (0, 0)$ in (3.2), or by integrating the spectral density over all wavenumbers

$$\langle u'_i u'_j \rangle(y) = \int \int E_{ij}(k_x, y, k_z) dk_x dk_z. \quad (3.3)$$

For a wall bounded flow in a full size domain, the low-wavenumber contributions to the Reynolds stress represent the mean influences of the large scale structures on the near wall dynamics. As is well known (Hutchins & Marusic 2007; Marusic *et al.* 2010; Lee & Moser 2017; Samie *et al.* 2018; Lee & Moser 2019), these low-wavenumber features of the near wall flow depend on Re_τ . In contrast, there is evidence that the high-wavenumber (small-scale) contributions to the Reynolds stress profiles are universal and independent of Re_τ (Samie *et al.* 2018; Lee & Moser 2019). By design, the NWP model's domain size does not allow accurate representation of the very large-scale structures known to exist in the near wall region, and thus one cannot expect its Reynolds stress profiles to agree with those computed from DNS (with the exception of the shear stress $\langle u'v' \rangle$, as discussed in section 3.1). Instead, one expects the NWP model to correctly capture the dynamics of the universal small scales elucidated by Samie *et al.* (2018) and Lee & Moser (2019) associated with the autonomous cycle of Jiménez & Pinelli (1999).

To determine whether or not this is the case, the model's spectra E_{ij} are compared to their DNS counterparts. The spectra are visualized in so-called log-polar coordinates (Lee & Moser 2019), in which the wavenumber magnitude $k = \sqrt{k_x^2 + k_z^2}$ is represented on a logarithmic scale. For fixed wall-normal location, the log-polar coordinates are defined as

$$\begin{aligned} k_x^\# &:= \frac{k_x}{k} \log_{10} \left(\frac{k}{k_{\text{ref}}} \right) \\ k_z^\# &:= \frac{k_z}{k} \log_{10} \left(\frac{k}{k_{\text{ref}}} \right) \end{aligned} \quad (3.4)$$

where k_{ref} is an arbitrary reference wavenumber that must be smaller than the smallest

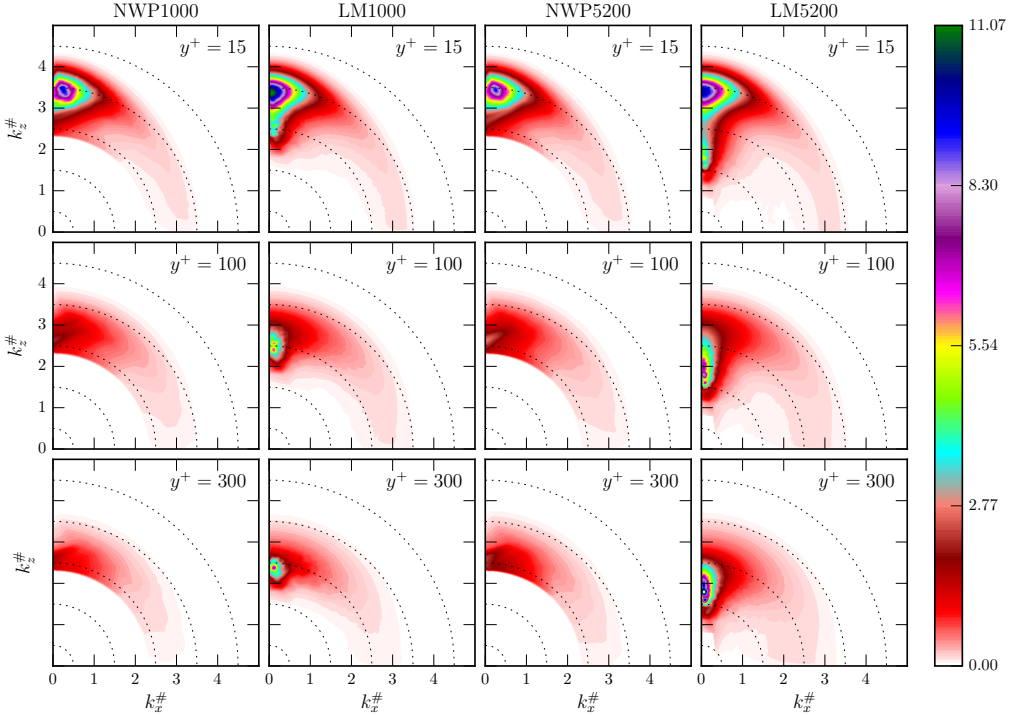


Figure 7: Two-dimensional spectra of the streamwise velocity variance $\langle u'u' \rangle^+$ in log-polar coordinates, as defined by equation (3.4). $\lambda^+ = 10$ on the outermost dotted circle and increases by a factor of 10 for each dotted circle moving inward.

nonzero wavenumber included in the spectrum, taken here to be $k_{\text{ref}}^+ = 1/50\,000$. Two advantages of these coordinates are that lines of constant k_z/k_x have slopes of k_z/k_x , and lines of constant magnitude k map to circles. In this way, the orientation and alignments of the Fourier modes are easily interpreted; see Lee & Moser (2019) for a more detailed discussion.

The two-dimensional spectral densities of the streamwise and wall-normal velocity variances are shown in figures 7 and 8, respectively. The spectra are visualized at the wall-normal locations $y^+ = 15$, $y^+ = 100$ and $y^+ = 300$ for the favorable pressure gradient simulations NWP1000, NWP5200, LM1000, and LM5200.

In each of the cases, the streamwise spectra E_{11} consist primarily of energy concentrated along the $k_z^{\#}$ axis, with Fourier modes for which $k_z/k_x \gtrsim 10$ (Lee & Moser 2019). These correspond to structures that are strongly elongated in the streamwise x -direction, such as the well-known, near wall low and high speed streaks. The channel flow data LM1000 and LM5200 (columns two and four in figure 7) show that this energy exhibits two distinct features. The first is an “inner energy site” (Samie *et al.* 2018), a triangular shaped region in the near wall layer $y^+ \approx 15$ distributed primarily between wavelengths $\lambda^+ = 100$ and $\lambda^+ = 1000$ that can be attributed to the autonomous near wall dynamics described by Hamilton *et al.* (1995); Jeong *et al.* (1997); Jiménez & Pinelli (1999), and others. The model E_{11} spectra, shown in columns one and three in figure 7, qualitatively reproduce the inner energy site, suggesting that it captures the dynamics of the near wall, small scale energetic motions.

The second feature is a concentration of energy at relatively low wavenumbers (in

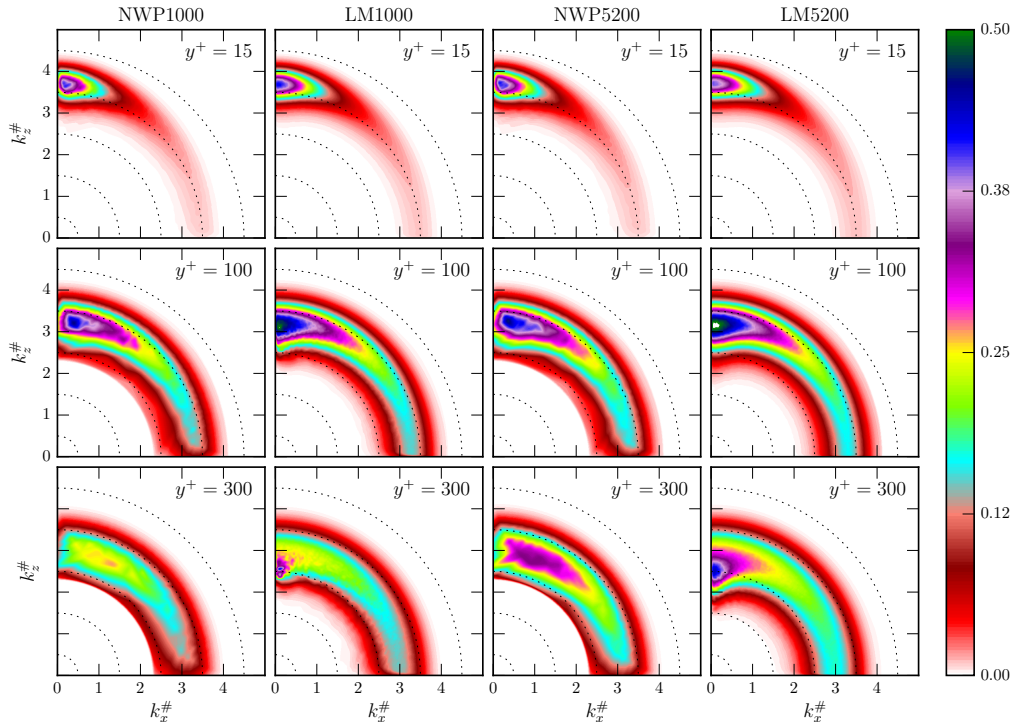


Figure 8: Two-dimensional spectra of the wall-normal velocity variance $\langle v'v' \rangle^+$ in log-polar coordinates, as defined by equation (3.4). $\lambda^+ = 10$ on the outermost dotted circle and increases by a factor of 10 for each dotted circle moving inward.

the range $1000 < \lambda^+ < 10000$) along the $k_z^\#$ axis at each of the wall-normal locations $y^+ = 15$, $y^+ = 100$, and $y^+ = 300$. These are due to the very large scale motions (VLSMs) imposed from the outer layer flow described by Hutchins & Marusic (2007) and Marusic *et al.* (2010). These VLSMs contribute energy in the near wall region around $y^+ = 15$, and farther away from the wall they are responsible for the majority of the turbulent kinetic energy. As both y^+ and Re_τ increase, the energy becomes more concentrated and is found at larger wavelengths, consistent with the attached eddy hypothesis of Townsend (1976). In addition, the VLSMs modulate the near wall cycle through nonlinear interactions, creating large scale variations in the local wall shear stress that result in local variations in the dominant (most-energetic) wavelength (Lee & Moser 2019). Consequently, the spectral peak of the inner energy site for the DNS data is reduced and “smeared out” as a function of Re_τ . For example, the $Re_\tau = 5200$ peak is about ten percent lower than the $Re_\tau = 1000$ peak.

By design, the NWP model can only support modes with wavelengths less than or equal to $L_x^+ = L_z^+ = 1500$, meaning the VLSMs present in real wall bounded turbulence are not represented by the model. As a result, there is no energy associated with such large scale structures; the concentration of energy at low wavenumbers along the $k_z^\#$ axis (corresponding to wavelengths $\lambda^+ \gtrsim 1000$) present in the DNS spectra is not present in that of the model. This is true both in the near wall region and farther away from the wall at $y^+ = 100$ and $y^+ = 300$.

Furthermore, the NWP model does not capture the nonlinear modulations of the

autonomous cycle by the VLSMs. For instance, even though the model represents wavenumbers along the $\lambda^+ = 1000$ band, its spectra is not simply a spectral truncation of the DNS spectra. Additionally, the peak of the inner energy site is nearly identical for the two model cases, differing by only a few percent. These differences between spectra of the model and DNS highlight the important role the VLSMs play in the turbulent near wall layer.

The E_{22} spectra are largest in the wavenumber regions in which the E_{11} spectra are peaked, as discussed in Lee & Moser (2019). Additionally, the distribution of energy generally becomes more isotropic with increasing wall-normal distance y^+ . Figure 8 shows that the DNS energy density E_{22} is primarily, but not exclusively, located at the small scales, i.e. at wavenumbers $\lambda^+ < 1000$. Because the NWP model adequately resolves such structures, its energy density E_{22} is in overall good agreement with the DNS spectra, especially in the near wall region. Farther away from the wall the agreement is not as good since the DNS spectra are peaked at lower wavenumbers. Accordingly, the model's unfiltered $\langle v'v' \rangle$ profiles shown in figure 10 show excellent agreement with the corresponding DNS profiles in region $y^+ \in [0, 300]$; they are nearly identical for $y^+ \lesssim 50$ and only display slight discrepancies for $y^+ \in [50, 300]$.

Lastly, fidelity of the NWP model's energy density E_{33} (not shown) in reproducing the DNS spectra is similar to the E_{11} spectra. It clearly approximates the small scales in the near wall region well, but it fails to capture the modulation by the large scale structures at each wall-normal location.

3.3. Universality of small scales

To better quantify the universality of the small scales and assess the NWP model's ability to reproduce them, the energy spectral density is high-pass filtered and then integrated to measure the energy residing in the small scales. Let \mathcal{K} denote the set of wavenumbers supported by a simulation, and let $k_{\text{cut}} = 2\pi/\lambda_{\text{cut}}$ with $\lambda_{\text{cut}}^+ = 1000$. Define \mathcal{K}_{SS} to be the subset of \mathcal{K} with the property that $(k_x, k_z) \in \mathcal{K}_{SS}$ if

$$\min\{|k_x|, |k_z|\} > k_{\text{cut}}, \quad (3.5)$$

visualized in figure 9 (left). The \mathcal{K}_{SS} sets are meant to contain large wavenumbers associated with the universal small scales. Here k_{cut} is chosen based on the two-dimensional spectra in Lee & Moser (2019), where it is observed that the energy associated with the autonomous cycle has $\lambda^+ < 1000$.

Note the high-pass filter (3.5) is slightly different than the L^2 filter

$$\sqrt{k_x^2 + k_z^2} > k_{\text{cut}} \quad (3.6)$$

used in Lee & Moser (2019) and visualized in figure 9 (right). In particular, the wavenumbers on the axis $k_x = 0$ (respectively $k_z = 0$) with $k_z > k_{\text{cut}}$ (resp. $k_x > k_{\text{cut}}$) are filtered out by (3.5) but not by (3.6). These axes contain the NWP model's approximation to the large scale motions present in a DNS that do not “fit” in the near wall patch domain. Such motions correspond to wavenumbers smaller than $2\pi/L_x = 2\pi/L_z$, and they are not well represented by the NWP model. Hence, they are filtered out by (3.5). The approximation can be improved by increasing L_x and L_z (confirmed by numerical tests), although this of course increases the model's overall computational cost.

Given \mathcal{K} and \mathcal{K}_{SS} , the Reynolds stresses are

$$\langle u'_i u'_j \rangle(y) = \sum_{(k_x, k_z) \in \mathcal{K}} E_{ij}(k_x, y, k_z), \quad (3.7)$$

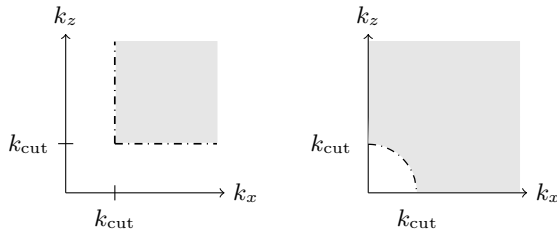


Figure 9: (Left) The shaded gray region indicates the subset (in the first quadrant) of wavespace \mathcal{K}_{SS} defined by (3.5). (Right) the corresponding region defined instead by the circular, L^2 filter (3.6) used in Lee & Moser (2019).

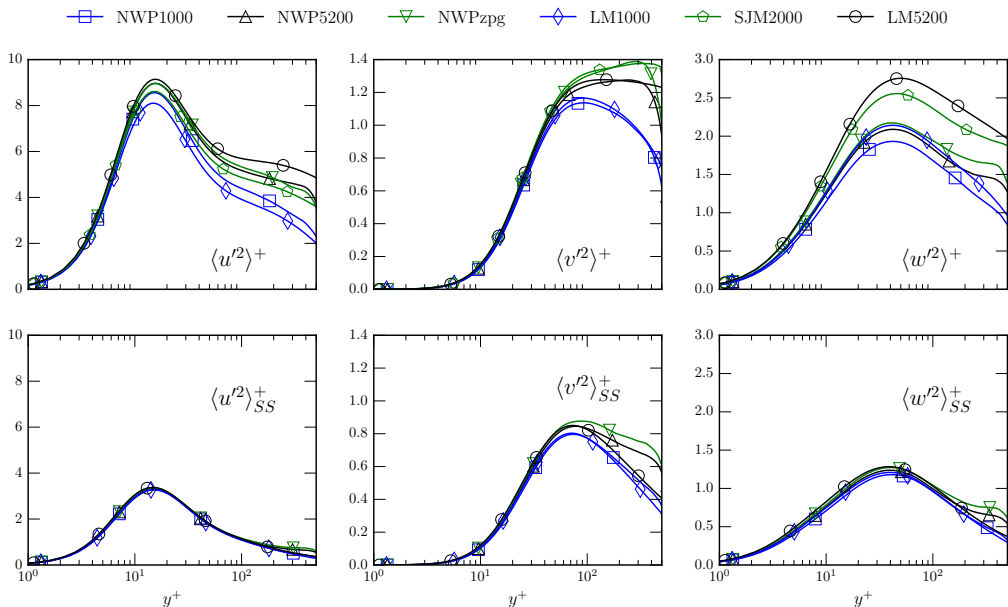


Figure 10: Velocity variances $\langle u'_\alpha u'_\alpha \rangle^+$ (top) and the corresponding high-pass filtered quantities $\langle u'_\alpha u'_\alpha \rangle_{SS}^+$ (bottom) as a function of $\log(y^+)$.

and the small scales energy can be quantified as

$$\langle u'_i u'_j \rangle_{SS}(y) = \sum_{(k_x, k_z) \in \mathcal{K}_{SS}} E_{ij}(k_x, y, k_z). \quad (3.8)$$

The velocity covariance $\langle u'v' \rangle$ and variances $\langle u'_\alpha u'_\alpha \rangle$, $\alpha = 1, 2, 3$ and their high-pass filtered counterparts are shown in figures 6 and 10, respectively. As previously mentioned, the model's unfiltered $\langle u'v' \rangle$ and $\langle v'v' \rangle$ profiles both agree quite well with the corresponding DNS profiles. The model's streamwise and spanwise velocity variances, however, display nontrivial discrepancies with the DNS profiles, as expected from the observed differences in the two dimensional spectra. In contrast, the model's high-pass filtered profiles all show excellent agreement with the high-pass filtered DNS quantities. In all cases the agreement is excellent in the region $y^+ \in [0, 100]$, although there are some relatively mild discrepancies for $y^+ \in [100, 300]$. Moreover, it is clear that the high-pass filtered quantities are nearly Re_τ independent; the collapse of the $\langle u'u' \rangle_{SS}$ profiles

is particularly convincing. Although two-dimensional spectra data is not available for the zero-pressure gradient DNS case SJM2000, the $\langle u'_i u'_j \rangle_{SS}$ profiles computed from the case NWPzpg are included for completeness; they display the same universal behavior as the favorable pressure gradient flows. These observations lend support to the conclusion that the small scales in the near wall region are universal, and that the difference in the Reynolds stress profiles as a function of Re_τ is due to the increasing influence of the VLSMs. Previous results of this type obtained in both Lee & Moser (2019) and Samie *et al.* (2018) involve high-pass filtering the *entire* turbulent flow field, in which there are nonlinear interactions between wavenumbers across all the scales of motion. It is particularly remarkable, however, that the NWP model reproduces the universal behavior of the small scales *without* the dynamic modulation of the near wall autonomous cycle by the large scale structures.

3.4. Production

The production of turbulent kinetic energy in a wall bounded flow is primarily due to the large mean velocity gradient in the wall normal direction $\partial U / \partial y$. In a flow that is homogeneous in the stream/spanwise directions with $V = W = 0$, the only $\langle u'_\alpha u'_\alpha \rangle$ term with a nonzero production is $\langle u' u' \rangle$; it is given by

$$\mathcal{P}_{11} = -2 \frac{\partial U}{\partial y} \langle u' v' \rangle. \quad (3.9)$$

The two dimensional spectra of \mathcal{P}_{11} is accordingly defined as

$$E_{11}^{\mathcal{P}}(k_x, y, k_z) := -2 \frac{\partial U}{\partial y}(y) E_{12}(k_x, y, k_z). \quad (3.10)$$

The spectral analysis of channel flow data in Lee & Moser (2019) demonstrated that in contrast to the near wall energy spectra E_{11} , the near wall production spectra $E_{11}^{\mathcal{P}}$ contains only a high wavenumber peak (see columns two and four in figure 11). It follows that the large scales in the near wall region, and hence the energy that they contain, are due to energy transport (either in y or in scale), rather than local production. This observation suggests that the NWP model should be able to capture the near wall energy production, even though the VLSMs are not present. The production spectra shown in figure 11 show that this is indeed true. At both $y^+ = 15$ and $y^+ = 30$, the NWP1000 and NWP5200 spectra are qualitatively similar to that of DNS, including the regions of negative production occurring over a range of scales around $\lambda^+ = 100$. Farther away from the wall, the large scale structures increasingly influence the energy production, and their influence increases with Re_τ . At $y^+ = 300$, the large scale influences dominate the DNS production spectra, and the model is not able to reproduce such low wavenumber features.

The one-dimensional, premultiplied production profiles are shown in figure 12, and they are consistent with the aforementioned observations regarding the two-dimensional spectra. The DNS profiles are approximately Re_τ -independent for $y^+ \lesssim 70$, the corresponding model profiles show strong agreement for $y^+ \lesssim 100$, and they begin to show modest discrepancies for $y^+ \gtrsim 200$.

3.5. Dissipation, pressure strain and transport

After being produced by the mean, turbulent kinetic energy is redistributed across scales and velocity components, transported both towards and away from the wall, and ultimately dissipated by viscosity. The relative strength, or importance, of these processes as a function of wall-normal distance can be measured by the terms in the Reynolds

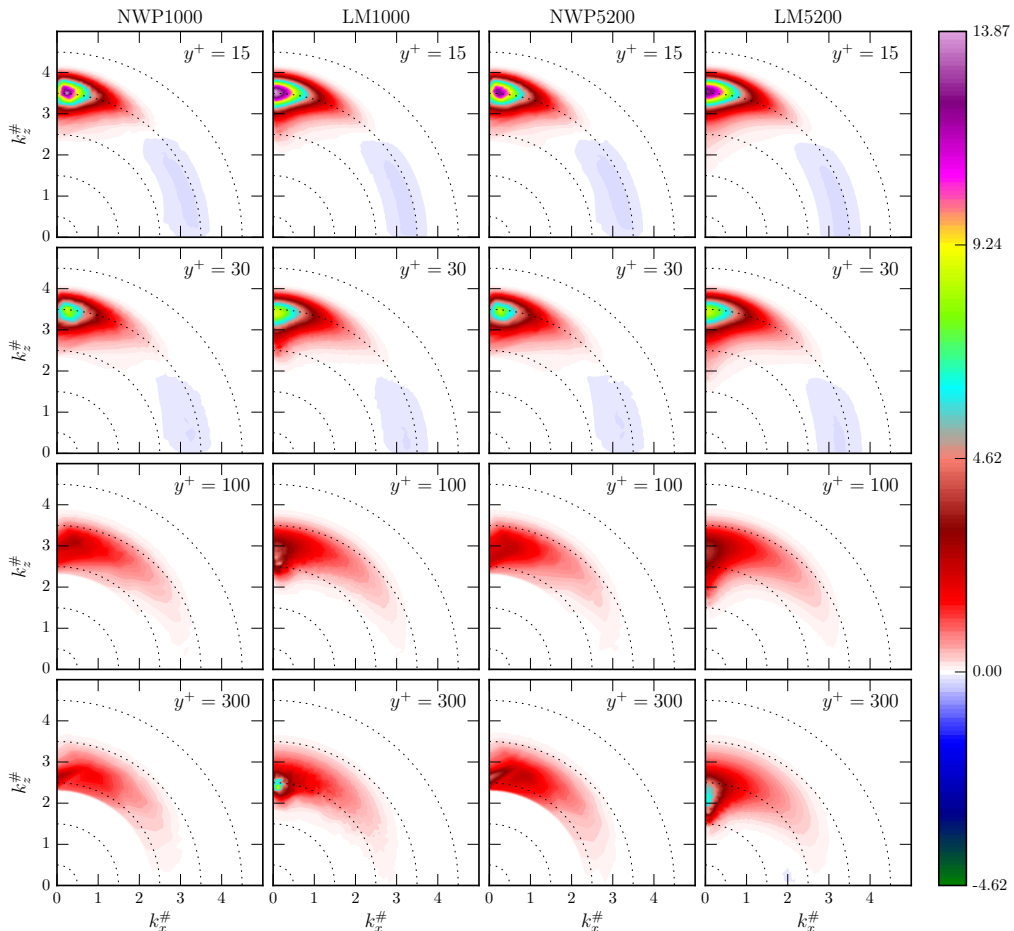


Figure 11: Two-dimensional, premultiplied spectra $y^+ (E_{11}^{\mathcal{P}})^+$ in log-polar coordinates, as defined by equation (3.4). $\lambda^+ = 10$ on the outermost dotted circle and increases by a factor of 10 for each dotted circle moving inward.

stress budget equation (Pope 2000). Exhaustive analyses of the behavior of these terms for wall bounded flows can be found in Hoyas & Jiménez (2008); Richter (2015); Mizuno (2015, 2016); Aulery *et al.* (2016); Lee & Moser (2019), and other references therein. A general conclusion to be drawn from these works is that, similar to the production and velocity variances, the small scale contributions to the terms in the budget equation are universal in the near wall region, and differences in the profiles as a function of Re_τ can be attributed to modulations by large scale motions. As a consequence, the terms in the budget equation produced by the model are seen to compare favorably with those produced by DNS in the region $y \in [0, 300]$. The model's premultiplied dissipation

$$\epsilon_{\alpha\alpha} = -2\nu \left\langle \frac{\partial u'_\alpha}{\partial x_k} \frac{\partial u'_\alpha}{\partial x_k} \right\rangle \quad (3.11)$$

profiles shown in figure 13, for example, are in good agreement with the corresponding DNS profiles in the range $y^+ \in [0, 100]$, show modest departures from the DNS profiles for $y^+ \in [100, 300]$, and completely diverge for $y^+ > 300$, as expected. The pressure

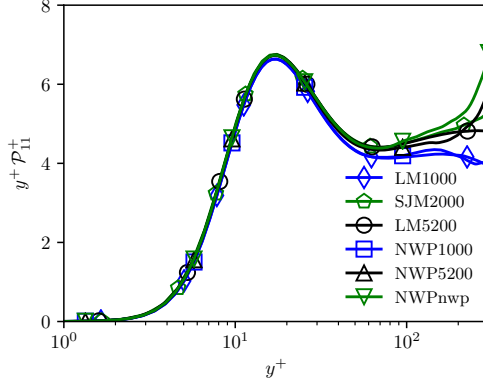


Figure 12: Profiles of the premultiplied $\langle u'u' \rangle$ production \mathcal{P}_{11}^+ versus $\log(y^+)$ in the region $y^+ \in [0, 300]$.

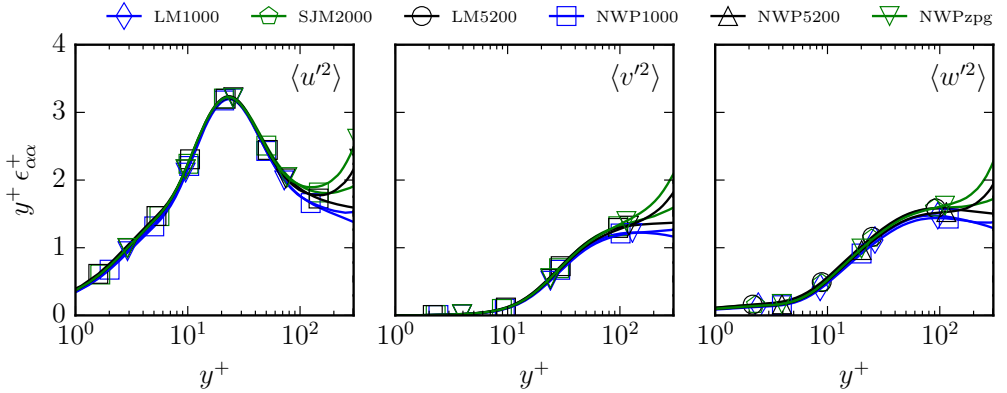


Figure 13: Profiles of $\langle u'^2 \rangle$, $\langle v'^2 \rangle$, and $\langle w'^2 \rangle$ dissipation as log densities.

strain and viscous, pressure, and turbulent transport terms (not displayed), all feature similar or better agreement than the dissipation profiles.

4. Conclusions

The near wall patch (NWP) computational model of wall bounded turbulence proposed here consists of a rectangular domain $\Omega = [0, L_x] \times [0, L_y] \times [0, L_z]$ whose size scales in viscous units. Similar to the simulations of Jiménez & Pinelli (1999), the NWP model seeks to isolate wall turbulence from the influence of very large scale motions present both farther away from and down to the wall. The model is cheap relative to a full DNS because it does not include wavenumbers associated with length scales larger than its domain size in the wall parallel directions, and is intended to simulate turbulence out to a wall normal distance of $L_y^+/2 = 300$. By assuming knowledge of the mean shear stress at the location $y = L_y$, the model accounts for the flux of mean momentum through the upper domain boundary in order to provide the correct “environment” for the near wall turbulence to evolve.

The primary modeling objective is to generate accurate near wall statistical quantities

as a function of pressure gradient. For both negligible and mild favorable pressure gradients, the mean velocities and their derivatives, the small scale contribution to the turbulent kinetic energy, and the production, dissipation and transport terms in the Reynold's stress budget equation are found to be in close agreement with the statistics from available DNS. However, for boundary layers with significant evolution of the mean quantities in the streamwise direction—such as those with adverse or strong favorable pressure gradients—a more refined model formulation appears to be required to account for the effect of boundary layer growth on the near wall fluctuations, for instance based on asymptotic expansions as in Spalart (1988).

Lastly, although not pursued in this study, the reduced order near wall patch model designed here could be used to economically perform numerical experiments on wall turbulence, as was done for example by Jiménez & Pinelli (1999) who tested dynamical theories of time-dependent near wall processes by modifying the equations of motion to suppress various candidate processes. A potentially valuable application could be to conduct relatively inexpensive computational studies of the interaction between near wall turbulence and more complicated physical processes such as heat transfer, chemical reactions, turbophoresis, or roughness effects.

5. Acknowledgments

The work presented here was supported by the National Science Foundation Award no. (DMS-1620396), as well as by the Oden Institute for Computational Science and Engineering. The research utilized the computing resources of the Texas Advanced Computing Center (TACC) at the University of Texas at Austin.

We wish to thank Myoungkyu Lee for assistance with the PoongBack code, supplying post-processing scripts for visualizing data, and insightful discussions. We also thank Todd Oliver, Prakash Mohan, and Gopal Yalla for insightful discussions and useful suggestions for this manuscript.

The authors report no conflicts of interest.

REFERENCES

- ABDULLE, ASSYR, WEINAN, E, ENGQUIST, BJÖRN & VANDEN-EIJNDEN, ERIC 2012 The heterogeneous multiscale method. *Acta Numerica* **21**, 187.
- AULERY, FREDERIC, DUPUY, DORIAN, TOUTANT, ADRIEN, BATAILLE, FRANCOISE & ZHOU, YE 2016 Spectral analysis of turbulence in anisothermal channel flows. *Computers and Fluids* .
- BERENDSEN, H. J. C., POSTMA, J. P. M., VAN GUNSTEREN, W. F., DiNOLA, A. & HAAK, J. R. 1984 Molecular dynamics with coupling to an external bath. *The Journal of Chemical Physics* **81** (8), 3684–3690.
- BERSELLI, L.C., ILIESCU, T. & LAYTON, W.J. 2006 *Mathematics of Large Eddy Simulation of Turbulent Flows*. Springer.
- BORRELL, GUILLEM, SILLERO, JUAN A. & JIMÉNEZ, JAVIER 2013 A code for direct numerical simulation of turbulent boundary layers at high Reynolds numbers in BG/P supercomputers. *Computers and Fluids* **80**, 37–43.
- BOSE, SANJEEB T. & PARK, GEORGE ILHWAN 2018 Wall-modeled large-eddy simulation for complex turbulent flows. *Annual Review of Fluid Mechanics* **50** (1), 535–561.
- BOTELLA, OLIVIER & SHARIFF, KARIM 2003 B-spline Methods in Fluid Dynamics. *International Journal of Computational Fluid Dynamics* **17** (2), 133–149.
- COLEMAN, G. N., GARBARUK, A. & SPALART, P. R. 2015 Direct Numerical Simulation, Theories and Modelling of Wall Turbulence with a Range of Pressure Gradients. *Flow, Turbulence and Combustion* **95** (2), 261–276.

- COLONIUS, TIM 2004 Modeling Artificial Boundary Conditions for Compressible Flow. *Annual Review of Fluid Mechanics* **36**, 315–345.
- DARCY, HENRY 1854 Recherches expérimentales relatives au mouvement de l’eau dans les tuyaux. *Mém. Savants Etrang. Acad. Sci. Paris* **17**, 1–268.
- DEGRAAFF, DAVID B. & EATON, JOHN K. 2000 Reynolds-number scaling of the flat-plate turbulent boundary layer. *Journal of Fluid Mechanics* **422**, 319–346.
- GANAPATHISUBRAMANI, B., HUTCHINS, N., MONTY, J. P., CHUNG, D. & MARUSIC, I. 2012 Amplitude and frequency modulation in wall turbulence. *Journal of Fluid Mechanics* **712**, 61–91.
- HAGEN, GHL 1839 Über den bewegung des wassers in engen cylindrischen röhren. *Poggendorfs Ann. Phys. Chem.* **46**, 423–42.
- HAMILTON, JAMES M., KIM, JOHN & WALEFFE, FABIAN 1995 Regeneration mechanisms of near-wall turbulence structures. *Journal of Fluid Mechanics* **287**, 317–348.
- HOYAS, SERGIO & JIMÉNEZ, JAVIER 2008 Reynolds number effects on the Reynolds-stress budgets in turbulent channels. *Physics of Fluids* **20**, 101511.
- HUTCHINS, NICHOLAS & MARUSIC, IVAN 2007 Large-scale influences in near-wall turbulence. *Philosophical Transactions of the Royal Society A: Mathematical, Physical and Engineering Sciences* **365**, 647–664.
- JEONG, J., HUSSAIN, F., SCHOPPA, W. & KIM, J. 1997 Coherent structures near the wall in a turbulent channel flow. *Journal of Fluid Mechanics* **332**, 185–214.
- JIMÉNEZ, JAVIER & MOIN, PARVIZ 1991 The minimal flow unit in near-wall turbulence. *Journal of Fluid Mechanics* **225**, 213–240.
- JIMÉNEZ, JAVIER & PINELLI, ALFREDO 1999 The autonomous cycle of near-wall turbulence. *Journal of Fluid Mechanics* **389**, 335–359.
- KHUJADZE, G. & OBERLACK, M. 2004 DNS and scaling laws from new symmetry groups of ZPG turbulent boundary layer flow. *Theoretical Computational Fluid Dynamics* **18**, 391–411.
- KIM, JOHN, MOIN, PARVIZ & MOSER, ROBERT 1987 Turbulence statistics in fully developed channel flow at low Reynolds number. *Journal of Fluid Mechanics* **177**, 133–166.
- KWOK, WAI YIP, MOSER, ROBERT D. & JIMNEZ, JAVIER 2001 A critical evaluation of the resolution properties of b-spline and compact finite difference methods. *Journal of Computational Physics* **174** (2), 510 – 551.
- LEE, MYOUNGKYU, MALAYA, NICHOLAS & MOSER, ROBERT D. 2013 Petascale direct numerical simulation of turbulent channel flow on up to 786K cores. In *the International Conference for High Performance Computing, Networking, Storage and Analysis*, pp. 1–11. New York, New York, USA: ACM Press.
- LEE, MYOUNGKYU & MOSER, ROBERT D. 2015 Direct numerical simulation of turbulent channel flow up to $Re_\tau = 5200$. *Journal of Fluid Mechanics* **774**, 395–415.
- LEE, MYOUNGKYU & MOSER, ROBERT D. 2017 Large-scale Motions in Turbulent Poiseuille & Couette flows. In *Tenth International Symposium on Turbulence and Shear Flow Phenomena*. Chicago, Illinois, USA.
- LEE, MYOUNGKYU & MOSER, ROBERT D. 2019 Spectral analysis of the budget equation in turbulent channel flows at high reynolds number. *Journal of Fluid Mechanics* **860**, 886–938.
- LEE, MYOUNGKYU, ULERICH, RHYS, MALAYA, NICHOLAS & MOSER, ROBERT D. 2014 Experiences from Leadership Computing in Simulations of Turbulent Fluid Flows. *Computing in Science Engineering* **16** (5), 24–31.
- MARUSIC, IVAN, MATHIS, ROMAIN & HUTCHINS, NICHOLAS 2010 High Reynolds number effects in wall turbulence. *International Journal of Heat and Fluid Flow* **31** (3), 418–428.
- MATHIS, ROMAIN, HUTCHINS, NICHOLAS & MARUSIC, IVAN 2011 A predictive inner–outer model for streamwise turbulence statistics in wall-bounded flows. *Journal of Fluid Mechanics* **681**, 537–566.
- MILLIKAN, CLARK B. 1938 A critical discussion of turbulent flows in channels and circular tubes. In *Proceedings of the fifth International Congress for Applied Mechanics*, pp. 386–392.
- MIZUNO, YOSHINORI 2015 Spectra of turbulent energy transport in channel flows. In *15th European Turbulence Conference*. Delft, The Netherlands.
- MIZUNO, YOSHINORI 2016 Spectra of energy transport in turbulent channel flows for moderate Reynolds numbers. *Journal of Fluid Mechanics* **805**, 171–187.

- MIZUNO, YOSHINORI & JIMÉNEZ, JAVIER 2013 Wall turbulence without walls. *Journal of Fluid Mechanics* **723**, 429–455.
- OLIVER, TODD A., MALAYA, NICHOLAS, ULERICH, RHYS & MOSER, ROBERT D. 2014 Estimating uncertainties in statistics computed from direct numerical simulation. *Physics of Fluids* **26**, 035101.
- PASCARELLI, ANDREA, PIOMELLI, UGO & CANDLER, GRAHAM V. 2000 Multi-block large-eddy simulations of turbulent boundary layers. *Journal of Computational Physics* **157** (1), 256–279.
- PIOMELLI, UGO & BALARAS, ELIAS 2002 Wall-layer models for large-eddy simulations. *Annual Review of Fluid Mechanics* **34** (1), 349–374.
- POPE, STEPHEN B. 2000 *Turbulent Flows*. Cambridge University Press.
- REYNOLDS, O. 1895 On the Dynamical Theory of Incompressible Viscous Fluids and the Determination of the Criterion. *Philosophical Transactions of the Royal Society of London Series A* **186**, 123–164.
- RICHTER, DAVID H. 2015 Turbulence modification by inertial particles and its influence on the spectral energy budget in planar Couette flow. *Physics of Fluids* **27** (6), 063304.
- SAGAUT, P., DECK, S. & TERRACOL, M. 2006 *Multiscale and Multiresolution Approaches in Turbulence*. Imperial College Press.
- SAMIE, M., MARUSIC, I., HUTCHINS, N., FU, M. K., FAN, Y., HULTMARK, M. & SMITS, A. J. 2018 Fully resolved measurements of turbulent boundary layer flows up to $Re_\tau = 20\,000$. *Journal of Fluid Mechanics* **851**, 391–415.
- SANDHAM, NEIL D., JOHNSTONE, RODERICK & JACOBS, CHRISTIAN T. 2017 Surface-sampled simulations of turbulent flow at high reynolds number. *International Journal for Numerical Methods in Fluids* **85** (9), 525–537.
- SILLERO, JUAN A., JIMNEZ, JAVIER & MOSER, ROBERT D. 2013 One-point statistics for turbulent wall-bounded flows at Reynolds numbers up to $\delta^+ \approx 2000$. *Physics of Fluids* **25** (10), 105102.
- SIMENS, MARK P., JIMNEZ, JAVIER, HOYAS, SERGIO & MIZUNO, YOSHINORI 2009 A high-resolution code for turbulent boundary layers. *Journal of Computational Physics* **228** (11), 4218 – 4231.
- SPALART, PHILIPPE R. 1988 Direct simulation of a turbulent boundary layer up to $Re_\theta = 1410$. *Journal of Fluid Mechanics* **187**, 61–98.
- SPALART, PHILIPPE R., MOSER, ROBERT D. & ROGERS, MICHAEL M. 1991 Spectral Methods for the Navier-Stokes Equations with One Infinite and Two Periodic Directions. *Journal of Computational Physics* **96**, 297–324.
- TANG, YIFENG & AKHAVAN, RAYHANEH 2016 Computations of equilibrium and non-equilibrium turbulent channel flows using a nested-les approach. *Journal of Fluid Mechanics* **793**, 709748.
- TOWNSEND, A. A. 1976 *The Structure of Turbulent Shear Flow*, 2nd edn. Cambridge University Press.
- WU, XIAOHUA & MOIN, PARVIZ 2009 Direct numerical simulation of turbulence in a nominally zero-pressure-gradient flat-plate boundary layer. *Journal of Fluid Mechanics* **630**, 5–41.
- YONG, XIN & ZHANG, LUCY T. 2013 Thermostats and thermostat strategies for molecular dynamics simulations of nanofluidics. *The Journal of Chemical Physics* **138** (8), 084503.